Journal of Power Sources 211 (2012) 4–11

Contents lists available at SciVerse ScienceDirect

Journal of Power Sources

journal homepage: www.elsevier.com/locate/jpowsour

Applying infrared thermography as a quality-control tool for the rapid detection of polymer-electrolyte-membrane-fuel-cell catalyst-layer-thickness variations

Niccolo V. Aieta [a], Prodip K. Das [b], Andrew Perdue [a], Guido Bender [a], Andrew M. Herring [c], Adam Z. Weber [b], Michael J. Ulsh [a,*]

[a] National Renewable Energy Laboratory, 1617 Cole Blvd., Golden, CO 80401, USA
[b] Lawrence Berkeley National Laboratory, 1 Cyclotron Rd., Berkeley, CA 94720, USA
[c] Colorado School of Mines, Department of Chemical and Biological Engineering, 1500 Illinois Ave., Golden, CO 80401, USA

ARTICLE INFO

Article history:
Received 9 December 2011
Received in revised form
10 February 2012
Accepted 11 February 2012
Available online 20 February 2012

Keywords:
Catalyst layer
Defects
Quality control
Infrared thermography
PEMFC
Fuel cell
Manufacturing

ABSTRACT

As fuel cells become more prominent, new manufacturing and production methods are needed to enable increased volumes with high quality. One necessary component of this industrial growth will be the accurate measurement of the variability of a wide range of material properties during the manufacturing process. In this study, a method to detect defects in fuel cell catalyst layers is investigated through experiment and mathematical simulation. The method uses infrared thermography and direct-current electronic-excitation methods to detect variations in platinum-containing catalyst-layer thickness with high spatial and temporal resolution. Data analysis, operating-condition impacts, and detection limits are explored, showing the measurement of defects on the millimeter length scale. Overall, the experimental and modeling results demonstrate great potential of this technique as a nondestructive method to measure defects that is amenable to use on roll-to-roll manufacturing lines.

1. Introduction

Materials and systems advances continue to improve the performance and durability of polymer electrolyte membrane fuel cell (PEMFC) systems, but cost continues to be a barrier to wider adoption [1]. However, PEMFC systems are currently being deployed in some early markets, and as this commercialization expands, there must be a transition from low-volume, largely manual manufacturing methods, to high-volume, continuous, and automated processes. In parallel, quality-control techniques must be developed that are sufficiently sensitive, rapid, noncontact, and nondestructive, and that can be implemented in continuous or automated production lines to inspect the entire material. Scalable quality-control methods are especially needed for membrane electrode assembly (MEA) components, including membranes, electrodes, and gas diffusion media (GDM), which are often inspected visually before use in a stack [2]. Of particular importance, given the high cost of Pt and other noble metal constituents, is the detection of variations in catalyst layers. Catalyst layer thickness variations, such as a spot with excessive or limited loading, can yield performance losses beyond those expected from the Pt-catalyst variation alone, especially at the local area near the defect [3–5]. This is most likely due to uneven compression of the GDM at the location of the defect, which increases resistance and leads to water management and other issues [5].

Today many MEA components are fabricated using roll-to-roll processes [2], wherein a sheet of material that is continuously formed by coating, casting, or other methods is conveyed through required process steps by a roller system, and wherein the final product is wound into a continuous roll (see [6,7] for details on general roll-to-roll processing). A large existing industry provides in-line inspection devices for typical roll-to-roll products such as adhesive tape and paper towels. These devices typically concentrate on optical inspection of visible defects or point measurements of coating thickness. Although these measurements can be extremely useful, they cannot necessarily be applied to PEMFC MEA components, because (1) not all defects are visible, particularly relative to the typically black, nonreflecting electrode coatings and GDMs; and (2) point measurements provide only statistical data – they generally cannot locate discrete defects, even if scanned across the sheet of material being fabricated, as is often done in the industry. Given

* Corresponding author. Tel.: +1 303 275 3842.
E-mail address: michael.ulsh@nrel.gov (M.J. Ulsh).

0378-7753/$ – see front matter © 2012 Elsevier B.V. All rights reserved.
doi:10.1016/j.jpowsour.2012.02.030

that discrete defects can act as failure-initiation points for MEAs in operation [8], an inspection technique must be developed that measures every location on the sheet material such that defects in MEA components can be removed prior to assembly into complete cells. This 100% inspection requirement is necessary to avoid premature cell failures, which often can cascade and cause complete stack failure and necessitate expensive stack replacement.

For catalyst layer defects, X-ray fluorescence (XRF) [9,10] has recently been applied to the in-line measurement of catalyst loading [11]. Unfortunately, this technique cannot at this time provide 100% inspection for catalyst layer defects. Acquisition times provided by commercially available systems to provide for quantitative analysis of Pt loading are on the order of 10 ms [12]. At these acquisition times, assuming a roll width of 18 in. and a web speed of 30 ft per minute, data are gathered only every 1.42 ft in the direction of substrate motion. Therefore, this technique can provide only a statistical metric of Pt.

Infrared (IR) thermography may enable complete, rapid (with response times on the order of 1 s for large areas), noncontact, and nondestructive detection of defects. In fact, several patents mention using IR thermography to detect various PEMFC parameters, including MEA and membrane defects [13–17]. However, little public information is available about the ability of specific excitation techniques to enable the detection of specific (size and type) defects in PEMFC materials. Although IR thermography techniques may not be element specific (as is XRF), this work shows that IR techniques can be used to identify catalyst layer thickness variations rapidly, at a relatively low cost, and with 100% inspection.

In this paper, a DC-based excitation technique is examined experimentally and theoretically for detecting variations in catalyst layer thickness via IR thermography (henceforth, IR/DC). As an initial study in the use of IR/DC detection for catalyst layer defects, this work focuses on detecting square spots of different thicknesses in a surrounding layer of nominal thickness. Assuming that Pt is uniformly distributed on the carbon support in the catalyst layer, this method allows for the quantification of the areal Pt loading using the known Pt/C ratio. Section 2 describes the experiment and theory for the technique. Section 3 presents the results of IR measurements with defined defects that are used for model validation. Section 4 uses experiments and modeling to examine the impact of different variables of the technique, including excitation time and voltage, and defect size and aspect ratio, as well as fuel cell testing data to verify that the technique does not damage the electrode material.

2. Experimental

Catalyst layer samples were prepared from a catalyst ink containing Ion Power Inc. DE2020 solution (20 wt% 1100 EW Nafion), n-propanol, water, and TKK Inc. TEC10E50E 46% Pt/Ketjen carbon catalyst. The ionomer to carbon mass ratio was 8:10. The total solids content in the ink was 6.8%. All components were hand mixed with a glass stir rod in a glass vial, sonicated for 4 h (in an ice bath), hand mixed, transferred to a 20-mL syringe, and horn sonicated for 30 s. The catalyst ink was then sprayed onto a 150-μm thick, 5-cm × 5-cm ethylene tetrafluoroethylene (ETFE) decal using a home-built ultrasonic spray system utilizing Sono-Tek's impact line of spray heads [18]. The spray system includes a syringe pump, a 120-kHz micro-bore spray head and power system, and a programmable x–y stage. Details of optimal conditions based on spray material can be found in [18]. The flow rates of the catalyst ink during spraying and the spray head conditions were optimized for the system to achieve a Pt loading of about 0.04 mg cm^{-2} in a single coat. The spray process was performed on a heated stage at 80 °C. No additional time for drying was needed between coats. Defects were made by applying a removable polymeric mask over a square region (typically 1 cm × 1 cm) in the center of the 25-cm^2 layer. The mask was removed during the deposition process to achieve the desired (lower) defect area thickness (loading). No residual adhesive remained after the mask was removed.

Fig. 1 shows schematics of the experimental setup and the experiment. Unless stated otherwise, a 21-V DC bias was applied to the setup using a Keithly 2400 source. For alternative voltages a BK Precision XLN 10014 Power Supply was used. Catalyst layer samples on the ETFE decals were fit between two brass clamps, which were clamped with two bolts torqued to 10 cm-kg$_f$. To detect the temperature variation, an IR camera (Jenoptik Vario-Cam HiRes) was used. The camera has a 640 × 480 pixels detector with accuracy under ±1.5 K. A uniform emissivity of 0.95 was used and was determined empirically by comparing a piece of 3 M brand masking tape, which has a known emissivity of 0.95 [19], at the same ambient conditions as the catalyst layer.

For cell testing, the defect-containing decals were hot-pressed onto Nafion 212 membranes at 130 °C under 120 lb$_f$-cm$^2_{\text{active area}}$ pressure for 5 min and assembled into cells using SGL25BC GDLs. Performance curves conducted after break-in were run with hydrogen and oxygen utilizations of 83% and 50% (1.2 and 2 stoich), respectively. Forward and then backward scans of the current from 0 to 996 mA cm^{-2} were executed in 6 increments with 15-min current holds at each point along the curve. The last 5 min of each data point were averaged for reporting.

3. Modeling

The development and analysis of the diagnostic technique was aided by mathematical modeling. For the computational models, the governing heat conduction and current conservation equations are:

$$\rho_i c_{p,i}\left(\frac{\partial T}{\partial t}\right) - \nabla\cdot(k_i\nabla T) = Q \tag{1}$$

and

$$-\nabla\cdot(\sigma_i\nabla\Phi) = 0 \tag{2}$$

respectively, where ρ_i, $c_{p,i}$, σ_i, and k_i are the density, specific heat capacity, electronic conductivity, and thermal conductivity of species i, respectively, T is the absolute temperature, t is time, and Φ is the electronic potential. The Joule heating rate per unit volume is computed from the dot product of the electric field and current density, $\boldsymbol{i}$,

$$Q_i = -\boldsymbol{i}\cdot\nabla\Phi \tag{3}$$

where the subscripts i in Eqs. (1)–(3) can be catalyst layer, ETFE decal, or catalyst layer defect.

The boundary conditions for the model are:

$$T = T_{\text{room}} \text{ and } V = V_{\text{applied}} \text{ for } \partial\Omega\in x = 0 \tag{4}$$

$$T = T_{\text{room}} \text{ and } V = 0 \text{ for } \partial\Omega\in x = w \tag{5}$$

$$n\cdot(-k_i\nabla T) = h_{\text{side}}(T - T_{\text{room}}) \text{ for } \partial\Omega\in y = 0 \text{ and } d \tag{6}$$

$$n\cdot\mathrm{J} = 0 \text{ for } \partial\Omega\in y = 0 \text{ and } d \tag{7}$$

$$n\cdot(-k_{\text{ETFE}}\nabla T) = h_{\text{bottom}}(T - T_{\text{room}}) \text{ for } \partial\Omega\in z = 0 \tag{8}$$

$$n\cdot(-k_{\text{CL}}\nabla T) = h_{\text{top}}(T - T_{\text{room}}) \text{ for } \partial\Omega\in z = h \tag{9}$$

where w, d, h are the width, depth, and height of the computational domain, respectively, and h_{side}, h_{top}, h_{bottom} are the convective heat transfer coefficients for the side, top, and bottom walls, respectively. The parameter values used in the numerical simulations are listed in Table 1, where the convection heat transfer coefficients are

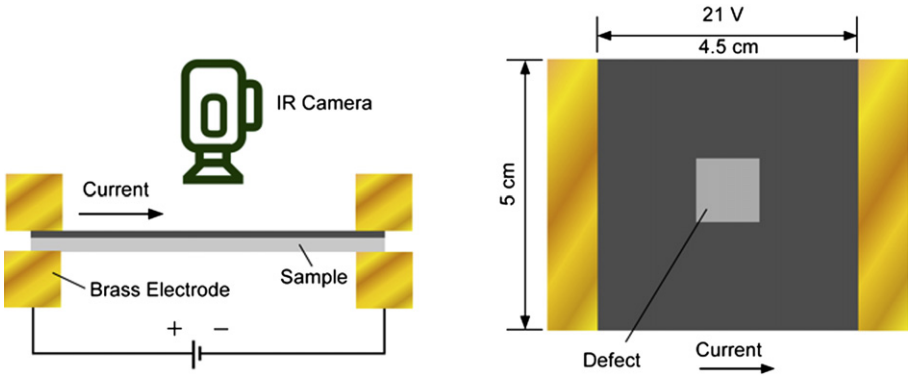

Fig. 1. DC-excitation/IR-thermography test setup and experiment for the detection of catalyst layer thickness variations. *Note*: the catalyst layer sample sits atop a decal that is suspended in air.

fitting parameters. In general, the convection heat transfer coefficient for air is 5–25 W m^{-2} K^{-1} for free convection and 10–200 W m^{-2} K^{-1} for forced convection. Therefore, the convection heat transfer coefficients used in this study indicate that the heat transfer from the catalyst layer was combined free and forced convection, which is reasonable considering that no significant measures were taken to isolate the experimental apparatus from the environment.

For the modeling domain, 3D and 2D domains were used; 3D provided higher resolution and 2D provided faster computation. Fig. 2 shows a schematic depiction of both computational domains (same as Fig. 1 with the brass clamps removed). The thermal effect of the brass clamps was accounted for using an isothermal boundary condition, and their effect on the numerical temerature profile was found to be negligible because the defect is located at the center of the sample. For the 2D model, the catalyst layer and ETFE decal layer were combined to form a composite layer (as shown in the middle part of Fig. 2) and then converted into a 2D domain (as shown in the bottom part of Fig. 2). An averaging scheme based on volume weighted properties was used to ensure that the results between the two models were consistent, as discussed in Appendix A. Although the 2D model is significantly faster than the 3D model, it provides the temperature distribution of the catalyst layer top surface only. If the temperature variation along the thickness of the catalyst layer is important, the 3D model is required.

The governing equations were solved using COMSOL Multiphysics. The 3D computational domain was discretized into a tetrahedral mesh, whereas the 2D computational domain was discretized into a triangular mesh, and adaptive mesh refinement was used to obtain better convergence. For both cases, second-order Lagrangian elements were used with the built-in direct solver MUMPS. The solutions were considered a converged solution when the preset tolerance value was below 10^{-6} and were mesh independent.

Table 1
Parameters used in the numerical simulations for the base case.

Parameter	Value	Unit	Source
w	25	mm	–
h	25	mm	–
σ_{CL}	3.12	S cm^{-2}	Measured
k_{CL}	2	W m^{-1} K^{-1}	[26]
ρ_{CL}	120	kg m^{-3}	[27]
$c_{p,\,CL}$	710	J kg^{-1} K^{-1}	[27]
k_{ETFE}	0.3	W m^{-1} K^{-1}	[28,29]
ρ_{ETFE}	1700	kg m^{-3}	[28,29]
$c_{p,\,ETFE}$	1047	J kg^{-1} K^{-1}	[28,29]
h_{top}	35	W m^{-2} K^{-1}	Fitting parameter
h_{bottom}	25	W m^{-2} K^{-1}	Fitting parameter

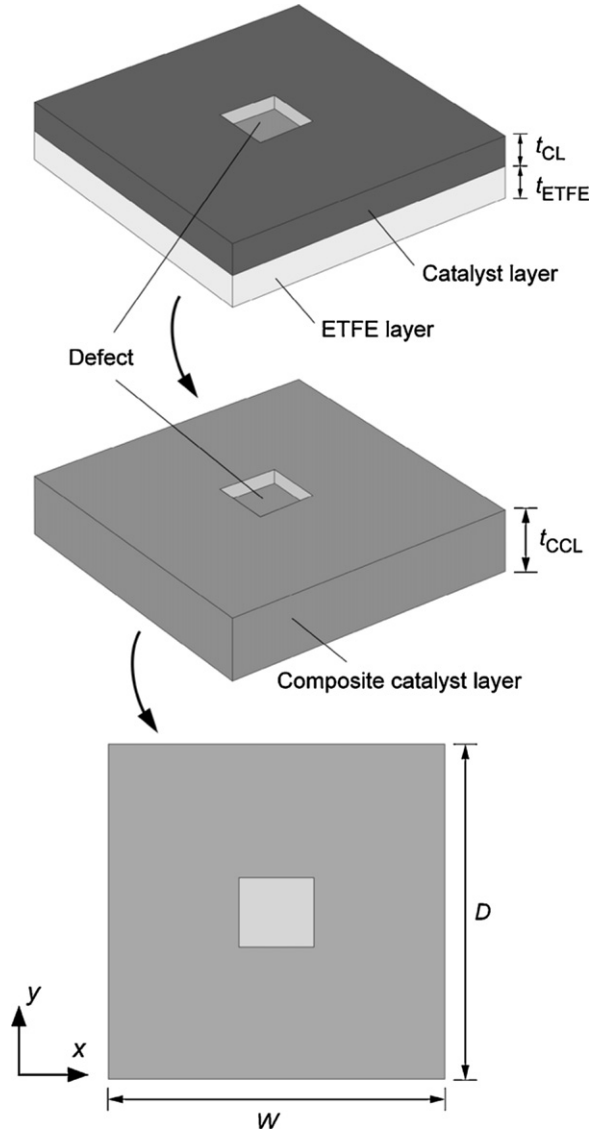

Fig. 2. Schematic depiction of the modeling domains. The top part shows the geometry used in the 3D model (a catalyst layer on an ETFE decal), the middle part shows an equivalent composite catalyst layer that is used to transform the 3D computational domain to a 2D domain whose properties can be estimated using the effective property formulation, and the bottom part shows the geometry used in the 2D simluation.

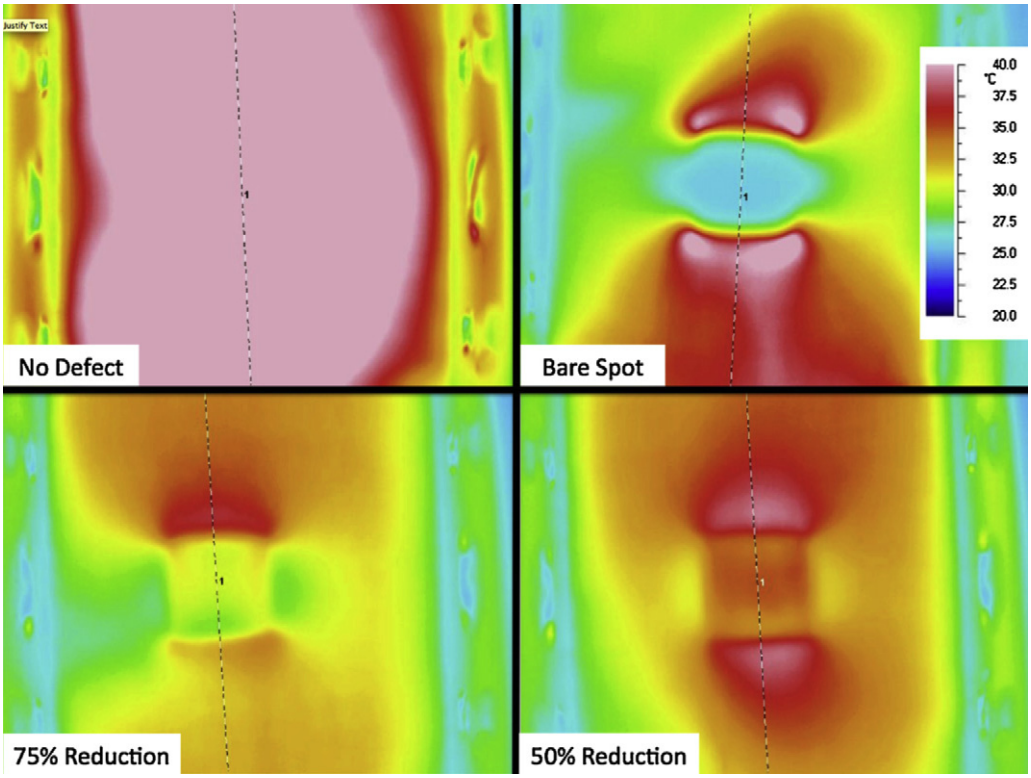

Fig. 3. False color thermal response of a pristine sample (100% loading), 100% reduction (bare spot), 75% reduction, and 50% reduction in catalyst layer thickness in the defect area.

4. Results and discussion

4.1. DC excitation and model validation

Fig. 3 shows IR thermographs of samples with 1-cm^2 square defects of different thicknesses (loading), excited under potentiostatic control at 21 V for 5 s. The current flows from left to right in each image. Thinner areas had lower overall temperatures than the thicker (standard) areas. The catalyst layer can be idealized as a mesh of resistors in which the current flow is governed by Ohm's law. In this scheme, the thinner areas lead to higher local in-plane resistances, resulting in lower current flow and temperature change. Because of the higher local resistances in the defect area, current preferentially flows around it, leading to a local temperature maximum just outside — in this case above and below — and a temperature drop inside the defect area. The temperature variations of the samples are statistically significant, i.e., outside the 90% confidence values of pristine samples.

Fig. 4 shows temperature line scans corresponding to the vertical lines in Fig. 3. These scans highlight quantitative differences that can be exploited to employ the IR thermography detection technique. The data allow three observations:

- Under potentiostatic control the overall temperature of any defect-containing sample is less than that for a pristine sample.
- The temperature differential near the edge of the defect increases with the severity of the defect because more current flows around rather than through the more electrically resistive defect area. This can be used to identify a defect, as it depends on many process variables, including defect size.
- Various data analysis methods may lead to the identification of a defect. For example, one can examine the absolute value of the temperature differential, or one can look at standard deviations along a temperature line scan. Fig. 5 illustrates an example for one possible data analysis method, which assesses the maximum temperature differential over each 0.2-cm increment along a line scan (hereafter referred to as $\Delta T/\Delta x$). Any value that is statistically relevant, i.e., higher than the 99% confidence limits around the pristine data, detects the defect. The figure demonstrates that for a 5-s, 21-V excitation, the detection size limits for a 10% and a 50% thickness (loading) reduction are 1 cm^2 and 0.0625 cm^2, respectively. We have previously shown that no detectable performance losses are seen for 1-cm^2 zero-loading defects 25-cm^2 CCM [11]. Our data suggests that we will be able to detect all catalyst loading variation defects that would result in detectable performance losses.

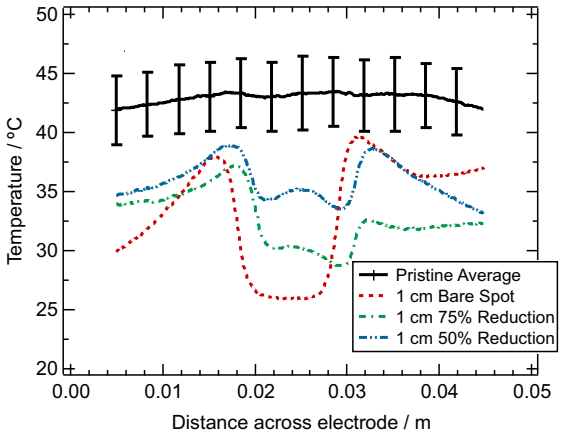

Fig. 4. Temperature profiles across a 25-cm^2 catalyst layer decal after 5 s of 21-V DC excitation. All samples contain a single 1-cm × 1-cm defect in the center of the sample with 100% (bare spot), 75%, or 50% reduction of the total catalyst layer thickness in the defect area. Error bars represent 90% confidence intervals for excitations on multiple pristine samples.

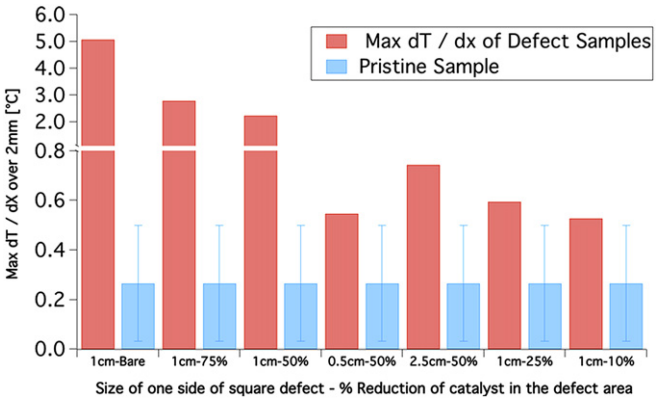

Fig. 5. Maximum temperature differential over a 0.2-cm spot size (with respect to position) across defect-containing and pristine samples after 5 s of 21-V excitation. Error bars represent 99% confidence values about the pristine samples. The *x*-axis indicates the length of one side of the square defect and the percentage of catalyst in the defect area for each sample.

Fig. 6 shows the comparison between model and experiment in terms of temperature profiles (Fig. 4) for two excitation times. The error percentages between the simulation and data are within a few percent or less near the defect region, thus validating the model. The numerical results do deviate from the experimental data at the edge of the samples, and this discrepancy can be explained by the assumption of the Pt-loading profile. An XRF line scan for a sample with a 25% thickness reduction in the defect area shows the Pt to be nonuniform, whereas the model assumes a step change at the defect and slight linear decreases away from the defect. The assumption of identical catalyst thickness profiles (defect and nondefect areas) along the *x*-direction is not necessarily valid and may explain the deviation between the data and the model.

4.2. Detection method and defect and variable exploration

As noted, the response time for implementing a diagnostic tool as a quality control technique for fuel cell-related roll goods is critical. The response time of the IR/DC method was explored experimentally and with the computer simulation. A 1 °C temperature variation was chosen as the metric for a successful defect detection and serves as an upper detection time bound. This metric is within camera resolution and is supported when comparing to the $\Delta T/\Delta x$ and a standard-deviation criterion, as it is outside the averages and confidence intervals for both. Fig. 7 shows experimental and simulated data for the time required to reach a 1 °C

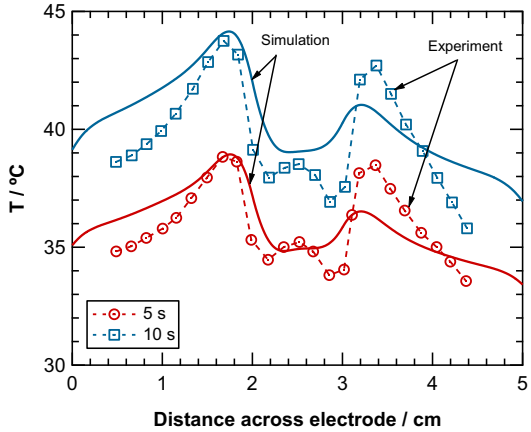

Fig. 6. Comparison of 3D simulation results with experimental data of the temperature profiles across the catalyst layer after 5 s and 10 s of 21-V DC excitation.

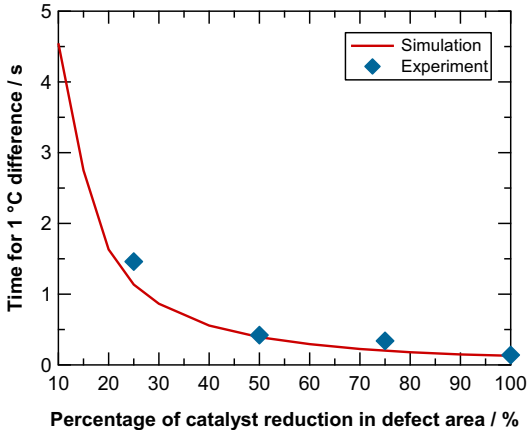

Fig. 7. Time for 1 °C temperature difference to be detected between the nondefect and defect areas. The solid line shows the prediction based on a 2D simulation for a 1-cm^2 defect with 21-V DC excitation.

temperature difference, using the $\Delta T/\Delta x$ data analysis method, to be detected between the pristine catalyst layer and the defect area. Excellent agreement between experimental and simulation data is shown. At the given excitation conditions, a bare spot can be detected in 0.2 s, whereas a 20% reduction in catalyst layer thickness in the defect area requires approximately 2 s for detection.

The standard deviation of the temperature along a line scan can also be used as an analysis method. The experimental error for pristine samples is shown as a black line in Fig. 8. Values above this line can be considered statistically significant for positive defect detection. The model was used to investigate this method for different defect sizes and thicknesses. The results demonstrate that a 20% reduction in catalyst layer thickness can be detected in less than 5 s for a 1-cm^2 defect size. However, for defects with smaller areas, only larger catalyst layer thickness variations will produce a detectable response. In fact, Fig. 8 shows that the standard deviation grows in a nonlinear and almost exponential fashion as the thickness in the defect area decreases. Using the $\Delta T/\Delta x$ instead of the standard deviation data analysis method allows for a faster detection of a smaller defect (see Fig. 7). The comparison between Fig. 7 and Fig. 8 highlights differences between the $\Delta T/\Delta x$ and standard deviation methods, and emphasizes the importance of the method used for analyzing the raw temperature data. The actual data analysis method used on a fuel cell roll good may further

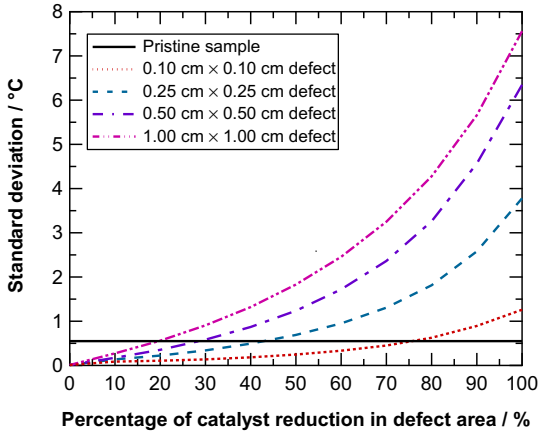

Fig. 8. Simulated standard deviation in temperature profile with defect loading after 5 s of 21-V DC excitation for different defect areas. The solid line indicates the experimental standard deviation in studies with pristine samples.

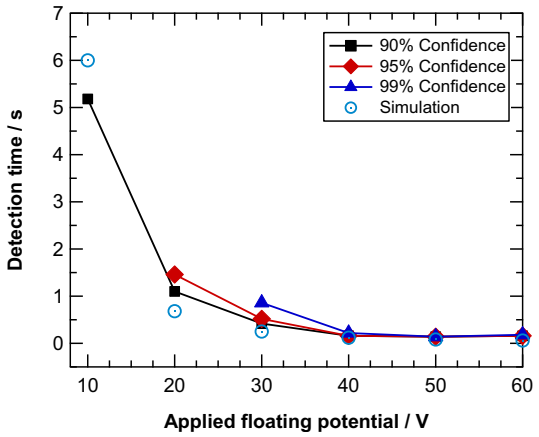

Fig. 9. Measured detection time for 1 °C temperature rise as a function of applied potential for a 0.25-cm^2 defect with 50% thickness reduction. Open symbols depict corresponding simulation results.

depend on the process control strategy and will be refined with respect to the kinds and sizes of defects that are expected on the manufacturing line. In actual operation, the time scale to perform these mathematical operations is expected to be such that both could be used.

Another critical process variable is the DC excitation voltage. This was explored through simulation and experiment, and results are shown in Fig. 9, where a catalyst layer with a 0.25-cm^2, 50% thickness reduction was excited with different voltages. In this figure, the time for detection is defined as the time at which $\Delta T/\Delta x$ along a line normal to both the defect edge and current flow was greater than 1 °C, which was outside the confidence levels determined for the pristine samples; this value is averaged over time (0.18 s) to account for noise. The data indicate that excitation voltages above 20 V result in detection times less than 1 s, and that above 30 V there is no additional gain in detection speed. The results shown in Fig. 9 indicate that the IR/DC method presented here is a valid candidate for rapid detection of catalyst layer thickness variations in fuel cell roll goods.

The validated model is run to determine the detection limits in terms of defect size and shape. Fig. 10 shows the temperature rise at the transition between the nominal catalyst layer and an area of 50% thickness reduction after 1 s and 3 s for a 21-V DC excitation as a function of defect size. The smallest defect size that can be detected within 1 s using the $\Delta T/\Delta x$ data analysis method is ~0.017 cm^2. However, by increasing the excitation time to 3 s,

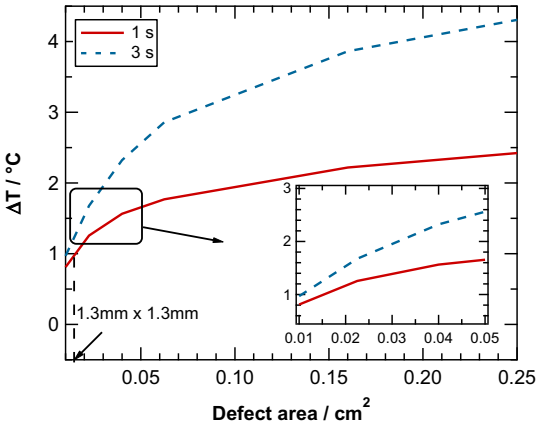

Fig. 10. Simulated temperature rise with time for a 21-V DC excitation as function of 50% thickness (loading) square defect.

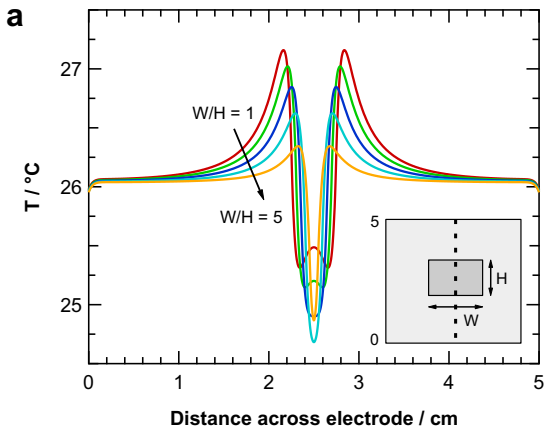

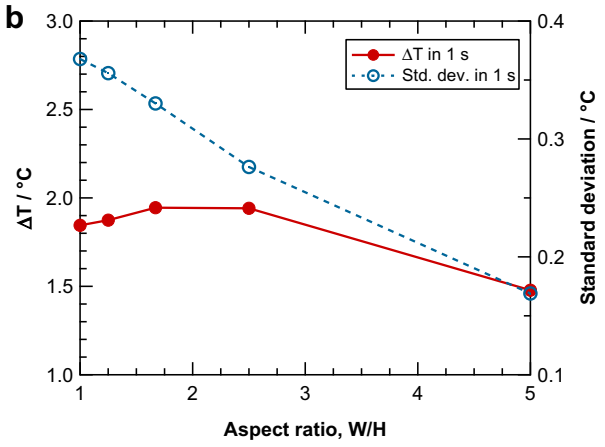

Fig. 11. (a) Temperature profiles across the electrode and (b) temperature rise between the defect and nondefect areas and standard deviation of the temperature profile as a function of aspect ratio after 1 s of 21-V DC excitation for 0.5-cm wide defects. The inset in (a) shows the definition of the aspect ratio.

a defect smaller than 0.01 cm^2 can be detected with the same criterion. The results also demonstrate a nonlinear dependence of the temperature rise with defect size, and indicate that the method is applicable over a wide range of defect sizes.

The effect of aspect ratio (*Width/Height* of defect) for a 0.5-cm wide defect was also explored using numerical simulation. Fig. 11a shows temperature profiles across the electrode along the dashed line, as indicated in the inset for different aspect ratios. The temperature profiles change significantly with aspect ratios, but the maximum-to-minimum variation in the temperature profile increases and then decreases with increased aspect ratio. This effect can be seen in Fig. 11b, where the solid line shows the maximum temperature variation between the defect and nondefect areas. Conversely, the standard deviation of the temperature profile monotonically decreases with aspect ratio, as indicated by the dashed line. Thus, using both methods at the same time can enable not only detection of a defect, but also (potentially) its shape.

4.3. Effects of DC excitation on fuel cell performance

A key attribute of any quality control technique is that it must be nondestructive to the sample. Thus, it is critical to know whether the high voltage applied during the measurement affects the performance and properties of the catalyst layers. For example, it is known that carbon corrosion (oxidation of carbon in the catalyst layer) occurs in an operating PEMFC, which can lead to

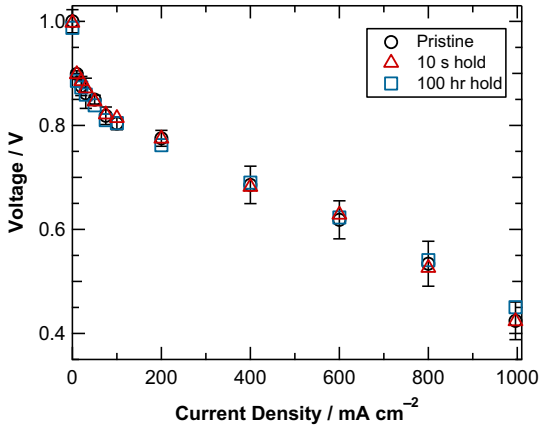

Fig. 12. Hydrogen/air polarization curves for pristine, 10-s, and 100-h DC-excited MEAs. Inlet conditions: 100%/50% relative humidity, 80 °C, 1 atm backpressure, 1.2/2.0 stoich. Error bars represent 90% confidence intervals based on repeat, pristine MEAs.

performance decrease due to loss of electrochemically active surface area (ECSA), when the cell potential is held above 0.8 V for periods of time [20–24]. To test the impact of the applied 21-V floating potential, a series of pristine and DC-excited samples were tested using polarization curves [25]. Fig. 12 shows hydrogen/air polarization curves for pristine and DC-excited catalyst-coated membranes (cathode side). Before being hot pressed into an MEA, the catalyst layers were subjected to 21 V in air at ambient temperature and humidity using excitation durations of either 10 s (the maximum time used in the quality control technique) or 100 h (to accelerate any effects). As illustrated in the figure, neither the 10-s hold nor the 100-h hold of the DC bias appeared to affect the MEA performance significantly. Table 2 gives the ECSA of the same set of samples, and shows that the ECSA of the voltage-held samples was not diminished.

Both the mass and thickness of the catalyst-coated decals excited for 100 h were measured before and after excitation. No changes were observed. Carbon corrosion can often lead to evolution of carbon oxides and can also lead to formation of glassy carbon, which is much denser than the porous carbon of a pristine catalyst [24]. Additionally, the in-plane resistance of the decals did not change over the 100-h experiment. Thus, no evidence of carbon corrosion or performance loss was found. When applied within the operating conditions reported here, the technique is noninterfering and nondestructive.

Table 2
ECSA for pristine and DC-excited MEAs.

Pristine samples	ECSA ($m^2\ g^{-1}$ Pt)
1	63.1
2	64.1
3	63.4
4	62.1
Average	63.2
90% confidence	1.3
DC-excited samples	**ECSA ($m^2\ g^{-1}$ Pt)**
1	68.8
2	69.3
3	74.3
Average	70.8
90% confidence	7.6

5. Conclusions

In this paper, a nondestructive, rapid technique to measure catalyst layer thickness variations, which can be correlated to Pt-loading variations, was introduced. The technique involves applying a DC excitation across a catalyst layer and measuring the thermal response using IR thermography. Experiments and modeling demonstrate that this technique can monitor small variations in thickness with temporal resolutions around 1 s or less. This technique was examined to understand the impact of defect size and shape, detection time, and applied voltage. Results show that higher voltages (<20 V) and longer times (~3 s) improve the defect size detection resolution to 0.01-cm^2 areas. In addition, various possible control and detection strategies were discussed. We conclude that this technique, in combination with electrified rolling electrodes, holds great promise for use as an on-line quality control method.

Acknowledgments

This work was funded by the Assistant Secretary for Energy Efficiency and Renewable Energy, Office of Fuel Cell Technologies, of the U.S. Department of Energy under contract numbers DE-AC36-08-GO28308 (NREL) and DE-AC02-05CH11231 (LBNL). P.K.D. also gratefully acknowledges financial support through a Natural Sciences and Engineering Research Council of Canada postdoctoral fellowship.

Appendix A

To decrease the computational cost of the simulations, a 2D effective property model was used instead of the full 3D one. In this 2D model, the properties can be defined as:

$$\sigma_{CCL}^{eff} = \frac{t_{CL}\sigma_{CL} + t_{ETFE}\sigma_{ETFE}}{t_{CL} + t_{ETFE}} \quad (A.1)$$

$$\sigma_{defect}^{eff} = \frac{t_{defect}\sigma_{CL} + t_{ETFE}\sigma_{ETFE}}{t_{defect} + t_{ETFE}} \quad (A.2)$$

where σ_{CCL}^{eff} is the effective electrical conductivity of the composite catalyst layer (combined layer of ETFE and catalyst layer), σ_{defect}^{eff} is the effective electrical conductivity of the defect area, t_{CL}, t_{ETFE}, t_{defect} are the thicknesses of the catalyst layer, ETFE layer, and defect, respectively, and σ_{CL}, σ_{ETFE} are the electrical conductivity of the catalyst layer and ETFE layer, respectively. The effective thermal conductivities can also be estimated using a similar approach, whereas the effective specific heat capacities for the composite layer and the defect region are defined as:

$$c_{p,CCL}^{eff} = \frac{t_{CL}\rho_e c_{p,CL} + t_{ETFE}\rho_{ETFE}c_{p,ETFE}}{t_{CL}\rho_E + t_{ETFE}\rho_{ETFE}} \quad (A.3)$$

$$c_{p,defect}^{eff} = \frac{t_{defect}\rho_{CL}c_{p,CL} + t_{ETFE}\rho_{ETFE}c_{p,ETFE}}{t_{defect}\rho_{CL} + t_{ETFE}\rho_{ETFE}} \quad (A.4)$$

respectively. The 2D model uses exactly the same set of governing equations as mentioned above, where the subscripts i represents the effective value of either the composite layer or the defect region as described in Eqs. (1) and (2). However, the source term in Eq. (3) is modified to account for the convective cooling from the top and bottom surfaces. The source terms for the 2D model are written as:

$$Q_{CCL} = -\mathbf{i}\cdot\nabla\Phi - \frac{h_{top}(T - T_{room}) + h_{bottom}(T - T_{room})}{t_{CL} + t_{ETFE}} \quad (A.5)$$

$$Q_{defect} = -\mathbf{i}\cdot\nabla\Phi - \frac{h_{top}(T - T_{room}) + h_{bottom}(T - T_{room})}{t_{defect} + t_{ETFE}} \quad (A.6)$$

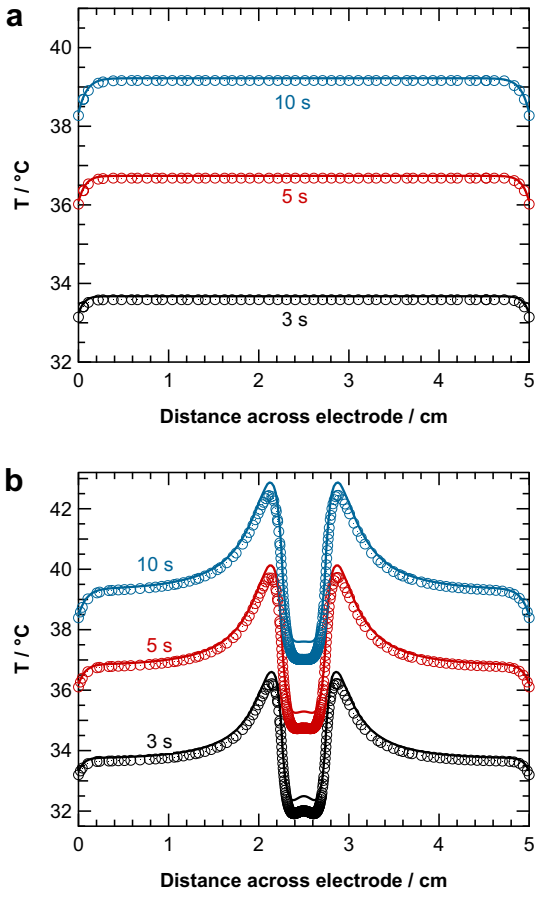

Fig. A1. Comparisons between 3D (line) and 2D effective-property (points) models for a (a) pristine and (b) 0.25-cm^2 50% thickness defect catalyst layer.

To ensure that the 2D and 3D models gave the same results, simulations were run and compared (see Fig. A1). From the figure, it is clear that the effective-property method agrees very well with the full 3D simulations in terms of transients and temperature profile. There is some undershoot in the temperature profile near the edges and in the middle of the defect; however, this is minor and is consistent such that the difference between the maximum and minimum temperatures is essentially identical in the two models.

References

[1] V. Mehta, J.S. Cooper, J. Power Sources 114 (2003) p32.
[2] DOE Multi-Year Research, Development and Demonstration Plan. http://www1.eere.energy.gov/hydrogenandfuelcells/mypp/pdfs/manufacturing.pdf.
[3] M. Pestrak, Y. Li, S.W. Case, D.A. Dillard, M.W. Ellis, Y.H. Lai, C.S. Gittleman, J. Fuel Cell Sci. Technol 7 (2010) 041009.
[4] S. Kundu, M. Fowler, L. Simon, S. Grot, J. Power Sources 157 (2006) 650.
[5] A.Z. Weber, J. Newman, J. Electrochem. Soc. 154 (2007) B405.
[6] E.D. Cohen, E.B. Gutoff, Modern Coating and Drying Technology, Wiley-Interscience, 1992.
[7] E.B. Gutoff, E.D. Cohen, G.I. Kheboian, Coating and Drying Defects Trouble-shooting Operating Problems, Wiley-Interscience, 2006.
[8] Y. Li, D.A. Dillard, S.W. Case, M.W. Ellis, Y.-H. Lai, C.S. Gittleman, D.P. Miller, J. Power Sources 194 (2009) 873.
[9] C. Wyon, D. Delille, J.P. Gonchond, F. Heider, L. Kwakman, S. Marthon, I. Mazor, A. Michallet, D. Muyard, L. Perino-Gallice, J.C. Royer, A. Tokar, Thin Solid Films 450 (2004) 84.
[10] C. Wyon, J.P. Gonchond, D. Delille, A. Michallet, J.C. Royer, L. Kwakman, S. Marthon, Appl. Surf. Sci. 253 (2006) 21.
[11] 2011 Annual Merit Review Proceedings – Manufacturing. http://www.hydrogen.energy.gov/annual_review11_manufacturing.html.
[12] High Speed, Low Cost Fabrication of Gas Diffusion Electrodes for Membrane Electrode Assemblies. http://www.hydrogen.energy.gov/pdfs/review10/mn007_decastro_2010_o_web.pdf.
[13] M.A. Sapia, J.G. Clark, U.S. Patent, Amdata, Inc., 1992.
[14] G.J. Lamont, D.P. Wilkinson, U.S. Patent, Ballard Power Systems Inc., 1998.
[15] M. Boehmisch, C. Haas, U.S. Patent, DaimlerChrysler AG, 2006.
[16] S. Roscoe, N. Rakow, R. Atanasoski, E. Jackson, J.H. Thomas III, L.H. McIntosh III, U.S. Patent, 3M Innovative Properties Company, 2006.
[17] M.W. Murphy, B.A. Litteer, U.S. Patent, General Motors Corporation, 2007.
[18] Sono-Tek Coating. http://www.sono-tek.com/energy/page/R&D.
[19] Emissivity Values. http://www.raytek.com/Raytek/en-r0/IREducation/EmisivityNonMetals.htm.
[20] K.H. Kangasniemi, D.A. Condit, T.D. Jarvi, J. Electrochem. Soc. 151 (2004) E125.
[21] A. Ofstad, J.R. Davey, S. Sunde, R.L. Borup, ECS Trans. 16 (2008) 1301.
[22] L.M. Roen, C.H. Paik, T.D. Jarvi, Electrochem. Solid State Lett. 7 (2004) A19.
[23] W. Schmittinger, A. Vahidi, J. Power Sources 180 (2008) 1.
[24] K.L. More, K.A. Perry, M. Chi, K.S. Reeves, in: Electrochemical Society Meeting Las Vegas (2010).
[25] US Fuel Cell Council – Single Cell Test Protocol. http://www.fchea.org/core/import/PDFs/Technical Resources/MatComp SingleCellTestProtocol05-014RevB.2071306.pdf.
[26] P.E. Khizhnyak, A.V. Chechetkin, A.P. Glybin, J. Eng. Phys. Thermophys. 37 (1979) 1073.
[27] Akzonobel, Product information: KetjenBlack EC-600JD, 2011.
[28] Fluorotherm, Product information: Ethylene tetrafluoro ethylene, 2011.
[29] DuPont, Production information: Tefzel fluoropolymer, 2011.